APPLICATIONS OF ALOS-PALSAR TO COASTAL WATERS WITH EXAMPLES OF SHIP DETECTION, AND INFORMATION EXTRACTION ON OCEAN WAVES AND UNDERWATER MARINE CULTIVATION

PI No : 232

Kazuo Ouchi [1] and Chan-Su Yang [2]

[1] Department of Computer Science, School of Electrical and Computer Engineering
National Defense Academy
1-10-20 Hashirimizu, Yokosuka, Kanagawa 239-8686, Japan.
Tel: +81 46 841 3810 ext. 3768, Fax: +81 46 844 5911, e-mail: ouchi@nda.ac.jp

[2] Korea Ocean Satellite Center, Korea Ocean Research and Development Institute,
1270 Sa2-dong, Sangnuk-gu, 426-744 Ansan, Republic of Korea.
Tel: +82 31 400 7678, Fax: +82 31 400 7606, e-mail: yangcs@kordi.re.kr

1. INTRODUCTION

ALOS (Advanced Land Observing Satellite) is, as the name suggests, primarily aimed at land observation, but it is also expected to take an important role in monitoring marine environment. In the present paper, applications of ALOS-PALSAR (Phased Array L-band Synthetic Aperture Radar) to monitoring the coastal waters are described with special emphasis on (1) detection of small ships by a novel technique based on CFAR (Constant False Alarm Rate) applied to multi-look cross-correlation coherence images, (2) detection of underwater laver cultivation areas by polarimetric entropy, and (3) waveheight estimation of range-traveling ocean waves using the polarization ratio.

2. SHIP DETECTION BY CFAR ON MLCC

For surveillance of piracy and ships responsible for oil pollution, as well as fishing control and navigation, several algorithms have been developed to detect, classify, and identify ships by SAR [1]-[5]. In the previous paper [6], we proposed a ship detection method from coherence images derived by cross-correlating multi-look SAR images. One of the problems in this MLCC (Multi-Look Cross-Correlation) algorithm is that it is difficult to set an appropriate threshold coherence value. The problem is overcome by applying CFAR to the MLCC coherence image.

2.1 Algorithm

The MLCC-CFAR algorithm is illustrated in the block diagram of Fig.1. An inter-look coherence image is first produced by cross-correlating look 1 and 2 images from

$$C = \frac{<A_1 A_2>}{<A_1><A_2>} - 1 \qquad (1)$$

using a moving window, where C is the inter-look correlation coefficient, A_1 and A_2 are look 1 and 2 image amplitudes respectively, and the angular brackets indicate taking an ensemble average. The size of the window for averaging depends on the size of ships of interest. For the present study, it was found the optimum size was 9 x 9 pixels.

The probability density function (PDF) which fits best to the coherence image is then sought based on the Akaike Information Criterion (AIC) [7], and the parameters of the PDF are calculated by the maximum likelihood estimation (MLE). Numerical integration is then carried out to decide the threshold value, and using this threshold value the coherence image is classified into 2 classes.

2.2 Experimental Description

To test this new algorithm, we carried out the experiments by cruising 3 different fishing boats of their lengths ranging from 8 to 15 m simultaneously with PALSAR observation in the Tosa Bay, Kochi, Japan during the Cal/Val period in 2006. The cruising speed was 8 knots (4.1 m/s) and the cruising direction is close to the range direction (8 degrees off-set from the range direction). The data were acquired in FBS 21.5, FBS 34.3, FBD 41.5, and PLR 20.5, where FBS, FBD, and PLR stand respectively for the Fine Beam Single, Fine Beam Double, and PoLaRimetric modes with the numbers indicating the off-nadir angles. The first 2 sets of data, where all 3 boats were visible, were used for the present study. The azimuth and slant-range resolution cells were 4.1 m and 4.7 m respectively.
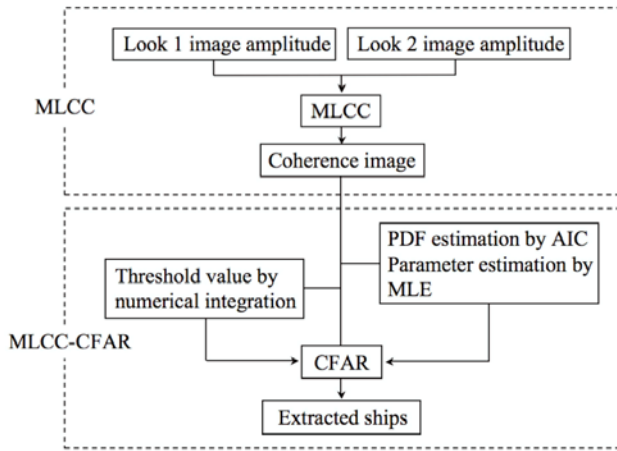
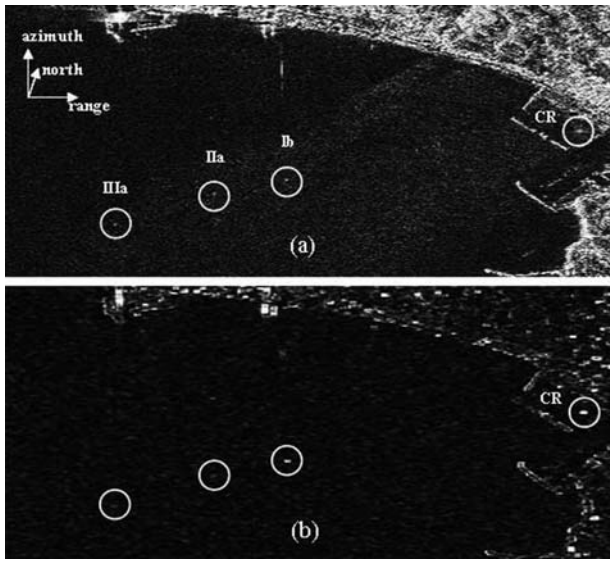**Fig. 1 Block diagram for MLCC-CFAR algorithm**

Fig. 2 The images (a) and (b) correspond respectively to the amplitude and coherence image after applying MLCC to the FBS 34.3 data.

The weather condition was such that the significant waveheights were 0.49 m and 0.35 m at the FBS 21.5 and 34.3 data acquisition times with the corresponding wind speeds 2.0 m/s and 1.0 m/sat the 10 m height.

2.3 MLCC Coherence Images

Fig.2 (a) and (b) show the HH-polarization amplitude image of the FBS 34.3 data and its MLCC coherence image respectively, where the white circles marked Ib, IIa, and IIa indicate the types of boat of length 14.6 m, 10.7 m, and 8.0 m respectively. The image marked "CR" at the centre-right is a triangular trihedral corner reflector of short-sided size 1.98 m (the theoretical Radar Cross Section (RCS) of 30.6 dB) placed on the beach for the purpose of PALSAR calibration. The image size of Fig.2 (a) is approximately 3.8 km in range direction, and 2.1 km in azimuth direction.

Fig.3 (a), (b), and (c) are the enlarged coherence images classified with threshold parameter N=2, 4, and 6 respectively, where N is defined by

$$C_T = <C> + N \cdot \sigma_C \qquad (2)$$

$<C>$ is the mean coherence magnitude, and σ_C is the standard deviation. It can be seen from Fig.2 (a)-(c) that the noises surrounding the images of boats decrease with increasing N, but the image of Type IIIa boat is thresholded out when $N = 6$. The best threshold may then be considered as $N = 4$ or 5. Thus, it is difficult to automatically determine the optimum threshold parameter for individual sub-scenes. To overcome this problem, the CFAR technique can be applied to the MLCC coherence images.
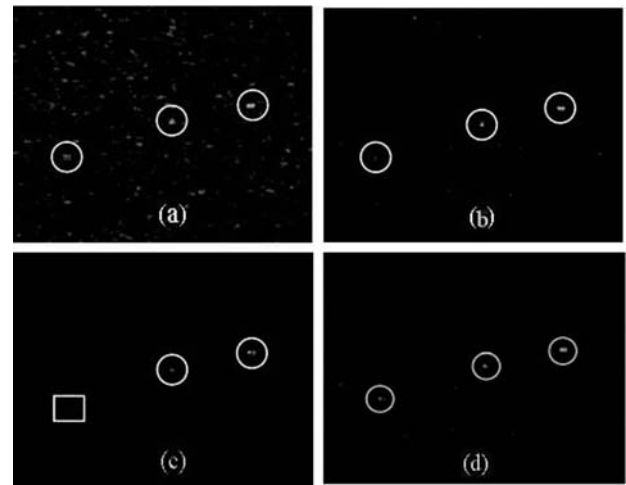

Fig. 3 The image (a), (b), and (c) are the enlarged coherence images after thresholding with the threshold parameter N=2, 4, 6 respectively. The image (d) is the coherence image after MLCC-CFAR. The white circles indicate the detected boats, while the white square implies an undetected boat.

2.4 Results of MLCC-CFAR

The new technique of MLCC-CFAR was applied to the 2-look coherence images of FBS 21.5 and 34.3 data following the steps shown in Fig.1. It was found that, for both the data sets, the amplitudes of individual multi-look images follow Weibull distribution [8], and the coherence image is described by the gamma distribution [9]

$$f(C; b) = \frac{C^{b-1}}{<C>^b \Gamma(b)} \exp\left(-\frac{C}{<C>}\right) \qquad (3)$$

where b is the shape parameter, and Γ is the gamma function. This result was found empirically and theoretical derivation is a subject of further research. The threshold coherence value can be found by setting the initial false alarm rate (FAR) in the following integral.

$$1 - \text{FAR} = \int_0^{C_T} f(C; b) \, dC \qquad (4)$$

The FAR value was set as 1×10^{-4} and 5.0×10^{-3} for the FBS 34.3 and 21.5 data respectively. The former FAR value was smaller than the latter because the FBS 34.3 image was less noisy than the FBS 21.5 image. Using this threshold value, the coherence image is classified as shown in Fig.3 (d) for the FBS 34.3 data as an example.

In order to compare the results in a more quantitative manner, FAR is computed in the MLCC-CFAR images as shown in Table 1. As can be seen in the table, the FAR in MLCC-CFAR images decreased in comparison with the simple threshold coherence images. It should be noted that for the FBS 21.5 data, the comparison should be made with MLCC with $N=2$ where all boats were visible as in the MLCC-CFAR image. The mean signal to background noise ratio over all three detected boats also improved to 56.8 dB for $N=4$ from 23.4 dB for $N=0$; and further improved to 66.0 dB after MLCC-CFAR. Similarly, for FBS 21.5, it increased to 27.1 dB for $N=2$ from 16.2 dB for $N=0$; and increased further to 34.9 dB after MLCC-CFAR.

Table 1 False Alarm Rate (Number of boats detected)

Modes	MLCC: $N=2$	MLCC: $N=4$	MLCC-CFAR
FBS 34.3	2.74×10^{-2} (3)	7.31×10^{-4} (3)	2.17×10^{-4} (3)
FBS 21.5	3.06×10^{-2} (3)	9.83×10^{-4} (2)	8.88×10^{-3} (3)

2.5 Summary

The technique of MLCC for ship detection is based on the strong correlation between the multi-look images of deterministic targets, *i.e.*, ships, and weak correlation of inter-look surrounding noise. It can extract images embedded in noise, but it is difficult to determine the correct threshold values. To overcome this problem, a simple technique is described to automatically determine the threshold value and to increase the accuracy of extracting ships by applying CFAR to the MLCC coherence images. ALOS-PALSAR data containing 3 small boats were used to test the proposed theory, yielding substantial improvement in FAR. Currently, a project is underway to integrate the several ship detection algorithms by SAR including the MLCC-CFAR with ground-based X-band radar equipped with the automatic identification system (AIS) in the Tokyo Bay, Japan.

3. DETECTION OF UNDERWATER OBJECTS BY POLARIMETRIC ENTROPY

Laver (*Porphyra*), which belongs to the algae group, is a popular seafood, particularly in Japan and Asia, and since it is rich in protein, dietary fiber, and vitamins, laver is also a source of mineral extract in medical industry. Laver cultivation is generally made in coastal waters, and monitoring such aquaculture is necessary for farming control, yield prediction, and damage assessment.

The attempts were made to extract and estimate the underwater laver cultivation nets using PALSAR PLR 21.5 images around the coastal waters of Futtsu Horn in Tokyo Bay, Japan. The principle of imaging underwater nets is the difference of surface roughness which depends on the water depth. Under low to moderate wind speeds, the water surface over the underwater nets placed at 10-20 cm below becomes smooth as the water is "effectively shallow", but the surface of "deep" water without nets is rough. This difference is difficult to detect by L-band SAR amplitude images as will be shown later. However, the polarization entropy can enhance the difference because of little backscatter from the smooth surface, resulting in the image composed of random system noise, that is, high entropy; while the backscatter from the deep sea is due to single-bounce surface scattering, *i.e.*, low entropy. In the following, a TerraSAR-X image of the test area is illustrated to show the difference in amplitude images of different wavelengths. Entropy analysis of PALSAR polarimetric data is then described, followed by the application of CFAR to the entropy images to estimate the area of cultivation nets.

3.1 TerraSAR-X Data

An aerial photograph of the cultivation area in Tokyo Bay is shown in Fig.4 where the underwater nets appear as dark rectangular patterns. The size of a single cultivation net is 123.0 x 8.3 m. These nets are placed in October at approximately 10-20 cm below the sea surface with supporting floats. Laver spores attached to the nets grow during winter, and the grown laver is harvested in April in the following year.

Fig. 5 is the TerraSAR-X SpotLight mode image acquired at 02:52 (UT) on December 26, 2008. The image size is approximately 5 x 5 km, and the resolution is 3.2 x 1.2 m in azimuth and slant-range directions respectively with incidence angle 21.2 degrees at the scene center.
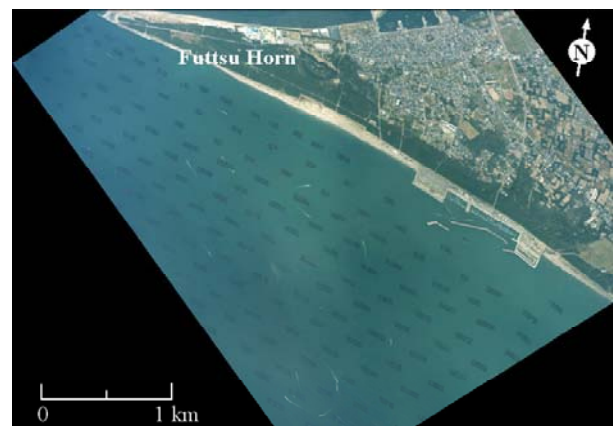

Fig. 4 Aerial photograph of the waters around the Futtsu Horn laver cultivation area taken on the 30th of November 1999. The photograph was provided by the Hydrographic and Oceanographic Department, Japan Coast Guard.
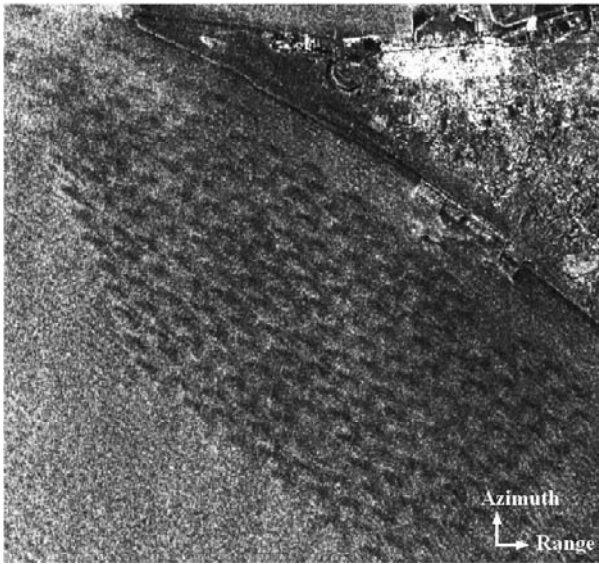
Fig. 5 TerraSAR-X HH-polarization image of the laver cultivation area. The dark patches correspond the the underwater laver cultivation nets.
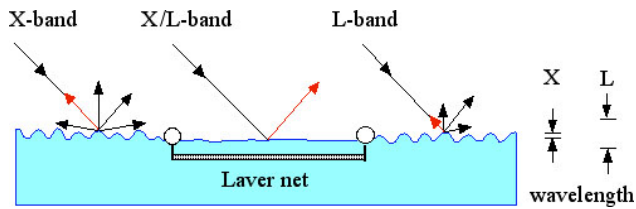

Fig. 6 The mechanism through which the underwater nets are imaged by SAR.

The significant waveheight of 0.6 m was provided by the Nationwide Ocean Wave information network for Port and HArbourS (NOWPHAS) acquired at a station located at approximately 3.8 km west from the cultivation area. The wind speed of 5.8 m/s was obtained at a station at approximately 9 km northeast from the observation site, and was supplied by the Japan Weather Association (JWA).

The process of imaging the underwater nets is illustrated in Fig.6. Since the cultivation nets are placed at 10-20 cm below the surface, the water is effectively "shallow", so that small-scale waves do not develop, and little radar backscatter is expected from this smooth surface. On the other hand, there is a certain amount of backscatter from "deep water" without nets. For a quantitative assessment, we define the mean contrast

$$V = \left| \frac{\langle A_{max} \rangle - \langle A_{min} \rangle}{\langle A_{max} \rangle + \langle A_{min} \rangle} \right| \qquad (5)$$

where A_{max} and A_{min} are the maximum and minimum mean amplitudes respectively. For the TerraSAR-X image the mean contrast was found to be 0.31 as shown in Table 2. The reason for this fairly good visibility is partly because of fine spatial resolution, but more importantly because the difference in radar backscatter between the smooth

and rough surfaces is large at X-band as illustrated in Fig.6. The visibility should then be lower in ALOS-PALSAR images since for L-band the open sea surface is "effectively" smoother than at X-band.

Table 2 Mean image contrast of amplitude and entropy images of underwater cultivation areas.

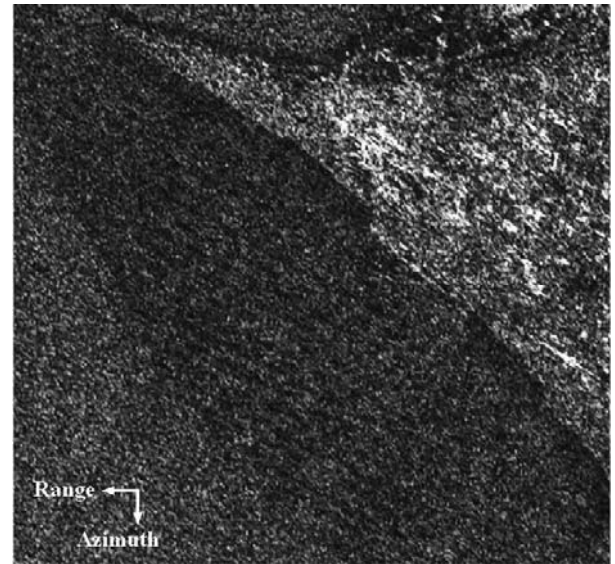| Sensors	ALOS-PALSAR (1)	TerraSAR-X	ALOS-PALSAR (2)
Amplitude	0.25	0.31	0.21
Entropy	0.56	N/A	0.47

Fig. 7 ALOS-PALSAR PLR 21.5 HH-polarization amplitude image of the laver cultivation area.

3.2 PALSAR PLR Data

Fig.7 shows the PALSAR HH-polarization amplitude image acquired at 01:20 (UT) on November 24, 2008. The images corresponding to the laver cultivation areas are not so clear as those of TerraSAR-X shown in Fig.5 with the mean contrast of 0.25 (ALOS-PALSAR (1) in Table. 2).

The amplitude PDF of the net area was found to be the Rayleigh distribution which is well-known to describe speckle amplitude fluctuations, and that of the deep water obeys Weibull distribution which is also known to describe sea clutter. The average RCS of the net area was approximately -22 dB. This value is close to the system noise of -23 dB. It can then be considered that the images of the net areas are composed predominantly by the random system noise, and those of the deep water by the single-bounce surface scattering. Polarimetric entropy may then be a good measure to show the difference in these scattering processes and hence to improve the image visibility.

Since the mathematical formulation of polarimetric entropy is well described [10]-[12], we present only the result of entropy image shown in Fig.8. Comparison with Fig.7 shows considerable improvement in image visibility.
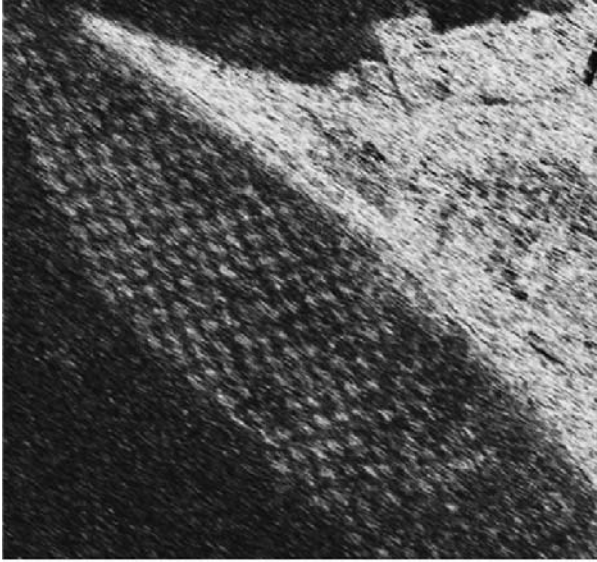
Fig. 8 Entropy image of PALSAR PLR data in Fig.7.

Fig. 9 Classified entropy image.

Indeed, the image contrast is more than twice the amplitude image as in Table 2 (ALOS-PALSAR (1)).
The analysis can be advanced a step further to classify and estimate the area of the cultivation nets. To do this, we applied CFAR to the entropy image. The procedure is the same as that shown in Fig.1 except that the coherence image is replaced by the entropy image. The PDF of the entropy image shown in Fig.8 was computed and found to follow the generalized extreme value (GEV) distribution

$$f(H;\mu,m,s) = \frac{1}{m}\exp\left(-(1+sz)^{-1/s}\right)(1+sz)^{-1-1/s}$$

(6)

where

$$z = \left(\frac{H-\mu}{m}\right)$$

(7)

and μ, m (>0), and s are the location, scale, and shape parameters respectively. This distribution is often used in risk analysis to describe rare meteorological events [13], and extreme fluctuations in share prices and foreign exchange rates in the field of economics [14]. For the entropy image in Fig.8, the MLE yielded μ=0.40, m=0.09, and s=-0.03. The threshold entropy of 0.389 was then calculated using the numerical integration of Eq.(4) by setting FAR=0.7. The initial FAR setting was again found empirically. Using this threshold entropy, the image of Fig.8 was classified as shown in Fig.9. The average area per single cultivation net computed from this classified image was 1096 m^2; while the "true" area was 1020.9 m^2, so that the accuracy was 93%. The same process was applied to the PALSAR PLR data acquired on the 12th of October 2009 (not shown in this paper) to yield the GEV distribution as the best-fitted distribution with μ=0.28, m=0.11, and s=0.11. By setting FAR=0.7, the threshold entropy was found as 0.268, and the estimated area par single net was 1163 m^2 with the accuracy of 86%.
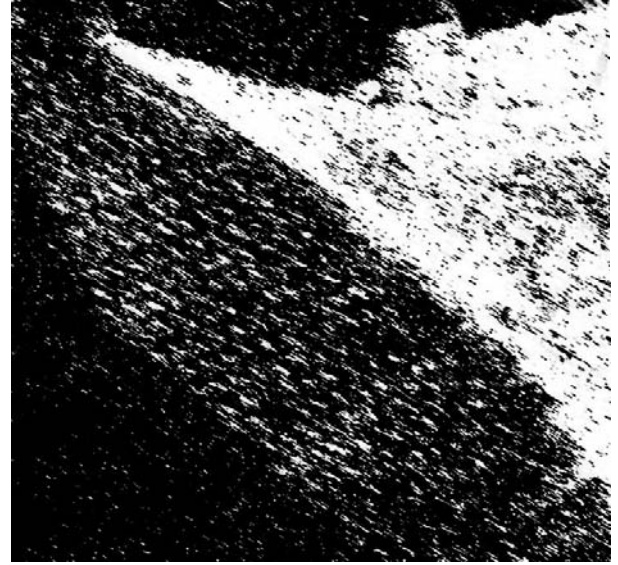
3.3 Summary

The polarimetric entropy was shown to be an effective parameter to extract the underwater laver cultivation nets, because the surface of the corresponding "shallow" water is smooth, and the image is dominated by the random process of system noise. Entropy is high in these areas as compared to the low entropy of deep sea surface from which the radar backscatter is dominated by the single-bounce surface scattering. Further details can be found in [15]. The principle can be applied to other oceanic phenomena such as classification of the surfaces covered by oil slick.

4. WAVEHEIGHT ESTIMATION BY POLARIMETRIC RATIO

Waveheight estimation of ocean waves by SAR is considered as very difficult due to several different imaging mechanisms depending on the look direction relative to wave propagating direction. To the authors' knowledge, the first attempt of waveheight estimation was by Thomas [16] who measured the waveheight of range-traveling waves from the difference in local incidence angle estimated using the composite-surface model in SEASAT-SAR HH-polarization RCS data in North Atlantic, resulting in overestimation by 20% due mainly to non-linear modulation by range bunching [17]. Since then, several models have been proposed, most of which are rather complex to use in practice (*e.g*., [18]).

In this paper, we propose a new simple technique to estimate the waveheight of range-traveling waves based on the dependence of the polarization ratio σ_{HH}/σ_{VV} on the local incidence angle, where σ_{HH} and σ_{VV} are the RCS at HH- and VV-polarizations respectively. The polarization ratio was originally used to estimate ocean

wind, and several empirical and semi-empirical models were proposed [19]-[22]. However, this relation can also be applied to estimate waveheight from its dependence of local incidence angle on the polarization ratio. The proposed method has an advantage over the previous methods (*e.g.*, [18]) for its simplicity and also over the single-polarization RCS method [16] since the non-linear multiplicative modulation by range bunching disappears by taking the radio, leaving only the RCS modulation (excluding hydrodynamic modulation).
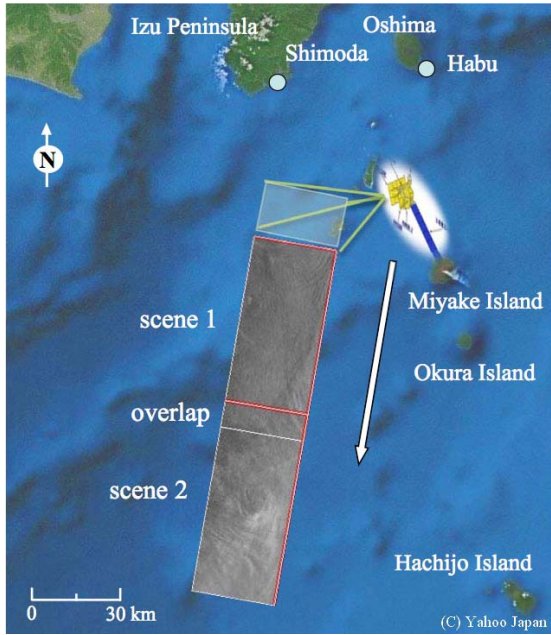

Fig. 10 Illustrating the areas used for the experiment.

4.1 SAR data and Polarization Ratio

The SAR data used in this analysis were acquired by ALOS-PALSAR at PLR 21.5 mode at 01:22 (UT) on September 5, 2006 over the waters south of Izu Peninsula, Japan as shown in Fig.10. The images were in the Level 1.1 processed by the Japan Aerospace Exploration Agency (JAXA). The spatial resolution is 5.5 m in azimuth and 23 m in ground-range directions. At the acquisition time, the typhoon 0612 was present in the Pacific Oceans about 1,000 km away from the northwest coast of Japan, and in the PALSAR images shown in Fig.10 there are substantial amount of wave images propagating predominantly in range direction.

First, we need to check the relation between the polarization ratio and incidence angles. The mean RCS was measured by averaging over the pixels in azimuth direction at a same range, and the polarization ratio was estimated as shown in Fig.11. It was found that this measured polarization ratio did not fit to any existing relations including those of Thompson *et. al.* [20] Vachon and Dobson [21], Kudryavtsev et. al. [22], and Mouche *et. al.* [23]. The discrepancy may well be because those previous formulations were based on C-band data.

Since no existing formulas were available, we computed the polarization ratio σ_{HH}/σ_{VV} which fits best to our data. There is a linear relation between the polarization ratio and the incidence angles with the following regression expression.

$$\frac{\sigma_{VV}}{\sigma_{HH}} = 22.12\,\theta - 8.534 \qquad (8)$$

where θ is the incidence angle. This relation is used to estimate the local incidence angle from the polarization ratio.
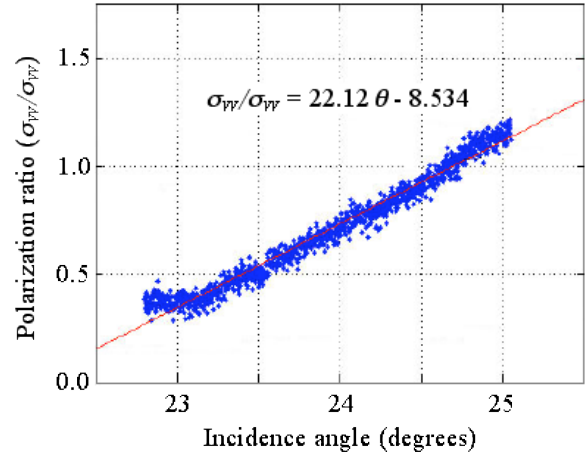

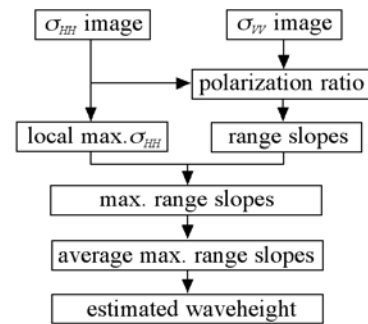**Fig. 11 Measured polarization ratio as a function of incidence angles.**

Fig.12 Flowchart of estimating ocean waveheight using the polarization ratio.

4.2 Estimation of Waveheight

The process of estimating the waveheight is illustrated in the flowchart of Fig.12. In principle, the spatial distribution of surface level can be computed by integrating over the spatial distribution of surface slope from the polarization ratio on a pixel basis. However, this approach did not have sufficient precision because of the large variations of polarization ratio. Therefore, we calculated the sea surface level in the HH-polarization image, and carried out the quantitative evaluation of the surface slope of range-propagating waves by computing

average maximum slopes, and approximating the swell images by a sine (or cosine) waves.

First, the intensity images of size 130 x 130 pixels (3 km x 3 km) consisting of predominantly range-traveling wave images in HH- and VV-polarization were selected. The polarization ratio was then calculated on a pixel basis, and from this ratio, local incidence angles were computed using Eq.(8). Local slopes were derived by subtracting the angle of incidence on the flat surface from the local incidence angles. These slope values contain fluctuations due to noise and local variation of actual wave slopes.

While, wave images of wavelengths between 100 m and 1,000 m were extracted by band-pass filtering the HH-polarization image. The pixels of largest σ_{HH} (5.75% of 130 x 130 pixels = 971 pixels) were then selected. These pixel positions correspond to largest surface slopes facing the radar. The slope values, θ_{max}, at these positions were found from those previously computed on the pixel basis. Note that the dominant wavelength was approximately 400 m, and the ground-range pixel spacing was 23 m; and hence the pixels 23/400 (6%) of largest slopes were selected from all pixels. The average surface slope $<\theta_{max}>$ was defined as the median value of θ_{max}. Since the dominant wavelength, L, is known from the image (through FFT spectral analysis), the dominant waveheight can be computed from

$$H = \frac{L}{2\pi} \tan(<\theta_{max}>) \qquad (9)$$

which can easily be derived from Fig.13.

We split the image into 3 km x 3 km areas and calculated the significant wave height for each area as shown in the upper image of Fig.14. In the lower of Fig.14 show the distribution of the estimated significant wave height, $H_{1/3}$, and wavelength. The estimated waveheight ranged from 0 m to 7 m, and the mean waveheight was 3.62 m. There exist some negative waveheight values because in these areas there are several wave patterns propagating in different directions.

The significant waveheights measured by the wave gauge of NAWPHAS in Shomoda and Habu were 1.5 m and 4.5 m respectively at the time 01:20 (UT) which is close to the PALSAR data acquisition time of 01:22 (UT). The JWA data showed the significant waveheight of 3.2 m in the offshore of Shimoda, and it was 4 m in the wave map by JWA. Thus, good agreement was obtained between the estimated waveheight and "sea truth" data.

4.3 Summary

The proposed technique of waveheight estimation appears to be promising for its simplicity with no effect of the non-linear range bunching modulation. The technique is limited to ocean waves traveling mainly in range direction, since the highly non-linear velocity bunching starts to take effect as the propagation direction tends to become azimuth. Further tests with more data may be required for the practical use of the proposed algorithm.
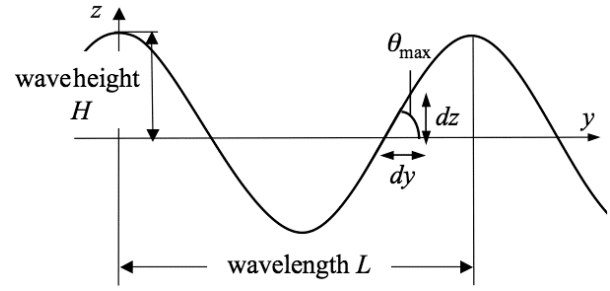

Fig. 13 Illustrating the ocean wave of a cosine (or sine) function, where y and z are the ground-range and vertical directions respectively.
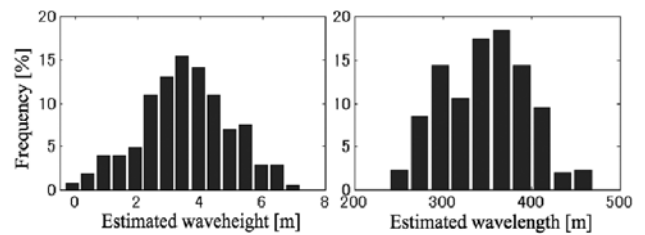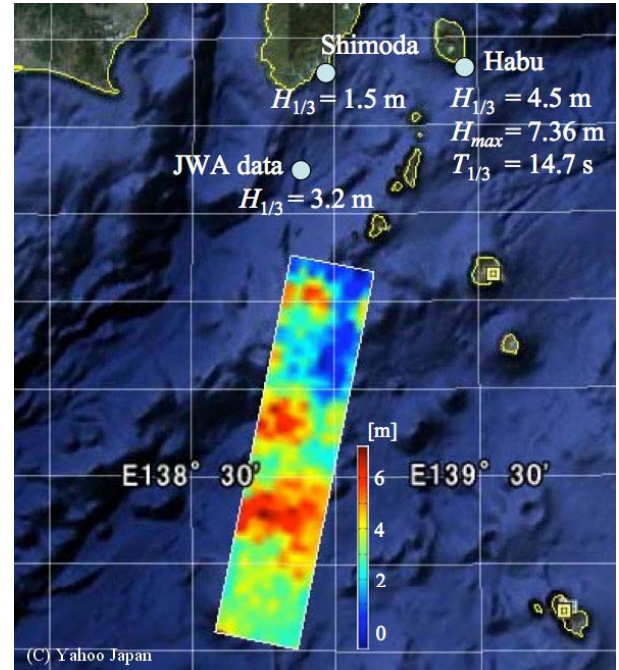

Fig. 14 Estimated significant waveheight (upper) and distributions of estimated waveheight and wavelength (lower).

5. CONCLUSIONS

In this paper, examples of ALOS-PALSAR applications to coastal waters were presented, which included small ship detection by MLCC-CFAR, detection and estimation of underwater laver cultivation nets by polarimetric entropy, and estimation of waveheight of ocean waves propagating in the directions around range by polarimetric ratio. All results showed good to reasonable agreement with sea truth data. As to the ship detection, further

experiments are being carried out in Tokyo Bay in order to develop a ship detection and identification system by integrating SAR, ground-based maritime radar and AIS. Polarimetric entropy was found to be an effective parameter to classify the underwater marine cultivation nets through the changes in surface roughness. The approach can also be used to monitoring other oceanic phenomena such as oil slicks. The technique of waveheight estimation by polarimetric entropy is particularly useful in coastal waters where the measurements by radar altimeters are difficult to use because of the coarse spatial resolution.

6. REFERENCES

[1] K. Eldhuset, "An automatic ship and ship wake detection system for spaceborne SAR images in coastal regions," *IEEE Trans. Geosci. Remote Sens.*, vol.34, pp.1010-1019, 1996.

[2] T.N. Arnesen and R.B. Olsen, *Literature Review on Vessel Detection*, FFI/RAPPORT-2004/02619, Forsvarets Forskningsinstitutt (Norwegian Defence Research Establishment), Kjeller, Norway, 2004.

[3] D.J. Crisp, *The State-of-the –Art in Ship Detection in Synthetic Aperture Radar Imagery*, DSTO-RR-0272, DSTO Information Sciences Laboratory, Edinburgh, Australia, 2004.

[4] K. Ouchi, S. Tamaki, H. Yaguchi, and M. Iehara, "Ship detection based on coherence images derived from cross-correlation of multilook SAR images," *IEEE Trans. Geosci. Remote Sens. Lett.*, vol.1, pp.184-187, 2004.

[5] H. Greidanus and N. Kourti, "Finding of the DECLIMS project-detection and classification of marine traffic control," *Proc. SEASAR 2006, Frascati, Italy (ESA SP-613)*, 2006.

[6] S-I. Hwang, H. Wang, and K. Ouchi, "Comparison and evaluation of ship detection and identification algorithms using small boats and ALOS-PALSAR," *IEICE, Trans. Commun*. vol.E92-B, no12, pp.3883-3891, 2009.

[7] H. Akaike, "Information theory and an extension of the maximum likelihood principle," *Proc. 2nd International Symposium on Information Theory*, pp.267-281, 1973.

[8] M. Sekine and Y. Mao, *Weibull Radar Clutter*, Peter Peregrinus, London, 1990.

[9] Seong-In Hwang and Kazuo Ouchi, "On a novel approach using MLCC and CFAR for the improvement of ship detection by synthetic aperture radar," *IEEE Geosci. Remote Sens. Lett.*, vol.7, no.2, pp.391-395, 2010.

[10] S.R. Cloude and E. Pottier, "A review of target decomposition theorems in radar polarimetry," *IEEE Trans. Geosci. Remote Sens.*, vol.34, no.2, pp.498-518, March 1996.

[11] S.R. Cloude and E. Pottier, "An entropy based classification scheme for land applications of polarimetric SAR," *IEEE Trans. Geosci. Remote Sens.,* vol.35, no.1, pp.68-78, Jan. 1997.

[12] Y. Yamaguchi, *Radar Polarimetry from Basis to Applications: Radar Remote Sensing using Polarimetric Information (in Japanese)*, IEICE (Corona Press), 2007.

[13] A.F. Jenkinson, "The frequency distribution of the annual maximum (or minimum) values of meteorological elements," *Quarterly J. Royal Meteorol. Soc.*, vol.81, no.348, pp.158-171, April 1955.

[14] T.G. Bali, "The generalized extreme value distribution," *Economics Letters*, vol.79, no.3, pp.423-427, June 2003.

[15] E-S. Won and K. Ouchi, "Estimation of underwater marine cultivation area based on SAR polarimetric entropy," *IEICE Tech. Rep.*, vol.110, no.250, pp.87-92, 2010.

[16] M.H.B. Thomas, "The estimation of wave height from digitally processed SAR imagery," *Int. J. Remote Sens.*, vol.3, no.1, pp.63-68, 1982.

[17] K. Ouchi, "Synthetic aperture radar imagery of range travelling ocean waves," *IEEE Trans. Geosci. Remote Sens.*, vol. GE-26, no.1, pp.30-37, 1988.

[18] K. Hasselmann and S. Hasselmann, "On the non-linear mapping of an ocean wave spectrum into a synthetic aperture radar image spectrum and its inversion," *J. Geophys. Res.*, vol.96, no.C6, pp.10,713-10,729, 1991.

[19] D.R. Thompson, T.M Elfouhaily, and B. Chapron, 1998. "Polarization ratio for microwave backscattering from the ocean surface at low to moderate incidence angles," *Proc.* 1998 *Int. Geosc. Remote Sen. Symp.*, pp. 1671–1673. 1998.

[20] P.W. Vachon and F.W. Dobson, "Wind retrieval from RADARSAT SAR images: selection of a suitable C-band HH polarization wind retrieval model. *Canadian J. Remote Sens.*, vol.26, no.4, pp. 306–313, 2000.

[21] V. Kudryavtsev, D. Hauser, G. Caudal, and B. Chapron, "A semiempirical model of the normalized radar cross-section of the sea surface 1. Background model," *J. Geophys. Res.* vol.108, no.C3, pp.2-20, 2003.

[22] A. Mouche, D. Hauser, V. Kudryavtsev, and J-F. Daloze, "Multi-polarization ocean radar cross section from ENVISAT ASTR observations, airborne polarimetric radar measurements and empirical or semi-empirical models," *Electronic Proc. 2004 Envisat & ERS Symp., 2004*.

[23] N. Shiroto, T. Tada, and K. Ouchi, "Estimating spatial distribution of oceanic waves using polarimetric synthetic aperture radar (in Japanese)," *JSCE J. Hydraulic Coastal Environ. Engineer.*, vol.66, no.1, pp.1416-1420, 2010.

[24] N. Shiroto and K. Ouchi, "Estimation of ocean waveheight using polarization ratio of synthetic aperture radar data," *Proc. 32nd Symp. Remote Sens.. Environ. Sci.,* pp.19-24, 2010.